Journal of Science and Transport Technology
Journal homepage: https://jstt.vn/index.php/en

UNIVERSITY OF TRANSPORT TECHNOLOGY

Pseudo-Lower-Bound Limit Analysis of Structures Using an Enhanced Cell-Based Smoothed Finite Element Method

Dung T. Tran[1], Canh V. Le[2,3], Phuc L. H. Ho[2,*]
[1]Faculty of Civil Engineering, Ho Chi Minh City Open University, Ho Chi Minh City, Viet Nam
[2]Faculty of Civil Engineering, HUTECH University, Ho Chi Minh City, Viet Nam
[3]School of Civil Engineering and Management, International University - VNU-HCM, Ho Chi Minh City, Viet Nam

Article info
Type of article:
Original research paper

DOI:
https://doi.org/10.58845/jstt.utt.2026.en.6.4.76-87

***Corresponding author:**
Email address:
hlh.phuc@hutech.edu.vn

Received: 15/12/2025
Received in Revised Form: 24/05/2026
Accepted: 24/06/2026

Abstract: Volumetric locking remains a major obstacle in pseudo-lower-bound limit analysis of near-incompressible structures. To overcome this difficulty, a bubble-enriched cell-based smoothed finite element approach is proposed, in which quadrilateral elements are supplemented with internal enrichment and the equilibrium constraints are imposed in a weak, spatially smoothed form over subcells. The resulting discrete problem is recast as a conic optimization model and solved efficiently using second-order cone programming (SOCP) techniques. Numerical examples confirm that the proposed approach effectively suppresses the locking behavior observed in the standard CS-FEM-Q4 formulation under near-incompressible plane-strain conditions. Computed solutions exhibit errors as low as 0.1% relative to analytical and reference results, while large-scale optimization problems can be solved within a few seconds. These results demonstrate that the proposed method provides an accurate, robust, and efficient computational tool for pseudo-lower-bound limit-state analysis, particularly for structures exhibiting near-incompressible behavior.

Keywords: Limit analysis; pseudo-lower-bound; Q5 element; CS-FEM; SOCP.

1. Introduction

Limit analysis offers a direct safety assessment by delivering the collapse load factor and mechanism without incremental load or time integration, making it attractive for design checks, optimization, and reliability studies. These quantities follow either directly from the classical static (lower-bound) and kinematic (upper-bound) theorems [1-3] or, as a special case under monotonic proportional loading, from the shakedown theorems [4, 5]. This foundation has enabled broad practical applications and catalyzed modern computational developments. Reliable realization of these variational formulations in practice, however, hinges on discretizations that remain accurate in near-incompressible regimes.

In two-dimensional plane-strain and three-dimensional analyses, volumetric locking can arise under near-incompressible conditions, where discrete constraints overconstrain dilatation, yielding overly stiff responses and slow convergence [6, 7]. Remedies include high-order finite elements [8, 9]; mesh-free approaches [10, 11]; mixed u–p formulations [12, 13]; discontinuous velocity fields [14]; simplex-strain elements [15]; reduced/selective integration within CS-FEM [16];

and enrichment strategies including ME-FEM and TLMR [17, 18], selective ES-FEM [19], and bubble-enriched linear schemes [20-24]. Preserving conformity, the five-node quadrilateral within CS-FEM achieves robust locking-free performance [25] and has recently been extended to the kinematic shakedown analysis framework [26].

This work aims to develop a robust locking-free, computationally efficient pseudo-lower-bound limit-state formulation based on CS-FEM-Q5. Each quadrilateral element is first enriched with a single bubble node, after which the cell-based smoothing is constructed over partitions to improve accuracy while mitigating volumetric locking. In this formulation, the total plastic stress field is decomposed into a fictitious elastic component associated with the collapse load multiplier and a residual stress, and the static equilibrium is imposed in a smooth weak form over the cell partitions. The resulting optimization problem is expressed as second-order cone programming (SOCP) and solved efficiently with modern conic optimizers (e.g., MOSEK). Numerical studies validate accuracy and convergence through mesh-refinement analyses and comparisons against reference solutions and baseline implementations.

2. Pseudo-lower-bound limit analysis

Let Ω denote a rigid-perfectly plastic body with boundary Γ split into a kinematic part Γ_u and a static (traction) part Γ_t, so that $\Gamma = \Gamma_u \cup \Gamma_t$ and $\Gamma_u \cap \Gamma_t = \varnothing$. The body is loaded by a traction field $\mathbf{f}$ on Γ_t. In this work, the pseudo-lower-bound limit load factor is derived from a special case of Melan's shakedown theorem [4] when the load domain reduces to a single vertex. Any stress field $\boldsymbol{\sigma}$ belonging to a space of statically admissible stress states $\mathcal{X}$ needs to lie in a convex set $\mathcal{B}$ defined by

$$\mathcal{B} = \left\{ \boldsymbol{\sigma} \in \mathcal{X} \mid \psi\left(\boldsymbol{\sigma}, \boldsymbol{\sigma}^{p}\right) \le 0 \right\} \tag{1}$$

with $\psi(\boldsymbol{\sigma}, \boldsymbol{\sigma}^{p})$ denotes the convex yield function, and σ^{p} is the yield stress of materials.

In the present static formulation, the total stress field is expressed as

$$\boldsymbol{\sigma} = \lambda \boldsymbol{\sigma}^{e} + \boldsymbol{\sigma}^{r} \tag{2}$$

where λ denotes the load multiplier, $\boldsymbol{\sigma}^{e}$ is the fictitious stress component, and $\boldsymbol{\sigma}^{r}$ is the residual stress. It is worth noting that, in the static formulation, the residual stress $\boldsymbol{\sigma}^{r}$ satisfies the equilibrium conditions, and the total stress field $\boldsymbol{\sigma}$ complies with the yield conditions for all possible load combinations everywhere within the problem domain as

$$\begin{aligned} &\nabla \boldsymbol{\sigma}^{r} = \mathbf{0} \\ &\psi\left(\lambda \boldsymbol{\sigma}^{e} + \boldsymbol{\sigma}^{r}, \sigma^{p}\right) \le 0 \end{aligned} \tag{3}$$

where ∇ is the gradient operator. This study adopts the classical von Mises yield condition, which can be written in the standard second-order cone form

$$\mathcal{C} = \left\{ \boldsymbol{\rho} \in \mathbb{R}^{n} \mid \rho_1 \ge \sqrt{\rho_2^2 + \rho_3^2 + \ldots + \rho_n^2} \right\} \tag{4}$$

where $\boldsymbol{\rho} = \left[\rho_1, \ \rho_2, \ \ldots \ \rho_n\right]^{T}$ is the additional variables.

Hence, a lower-bound limit load factor can be obtained from the optimization program

$$\begin{aligned} &\lambda^{-} = \max \lambda \\ &\text{s.t.} \quad \begin{cases} \nabla \boldsymbol{\sigma}^{r} = \mathbf{0}, \\ \boldsymbol{\rho}(\mathbf{x}) \in \mathcal{C} \quad \forall \mathbf{x} \in \Omega. \end{cases} \end{aligned} \tag{5}$$

From a numerical standpoint, equilibrium is enforced at finitely many integration points; however, the governing equations require satisfaction over the entire domain. To overcome this difficulty, the principle of virtual work is used so that the equilibrium requirement is imposed in a weak sense

$$\int_{\Omega} \delta \boldsymbol{\varepsilon}^{T} \boldsymbol{\sigma}^{r} \, d\Omega = 0 \tag{6}$$

where $\delta \boldsymbol{\varepsilon}$ is a kinematically admissible virtual strain field that satisfies the prescribed displacement boundary conditions.

Accordingly, the pseudo-lower-bound formulation can be recast as

$$\lambda^{-} = \max \lambda \tag{7}$$

$$\text{s.t.} \quad \begin{cases} \int_{\Omega} \delta\boldsymbol{\varepsilon}^{T}\boldsymbol{\sigma}^{r}\, d\Omega = 0, \\ \boldsymbol{\rho}(\mathbf{x}) \in \mathcal{C} \quad \forall \mathbf{x} \in \Omega. \end{cases}$$

3. Enhanced cell-based smoothed finite element methods

3.1. Conforming shape function for Q5-element

Following the five-node ME-FEM-GI concept of Wu et al. [17], the proposed Q5-element adopts a bubble-type enrichment inspired by incompatible-element theory [27] to define the shape function associated with the fifth node; however, unlike classical incompatible bubbles, this additional node N_5 carries physical displacement DOFs, so both the displacement approximation and the nodal geometry remain conforming. The parent domain is the square $\Omega_e = [-1, 1] \times [-1, 1]$ with corner nodes N_1, N_2, N_3, N_4 and a central node N_5. The physical element is obtained through the iso-parametric mapping

$$\mathbf{x} = \mathbf{F}_e(\boldsymbol{\xi}) = \sum_{i=1}^{5} \psi_i(\boldsymbol{\xi})\mathbf{x}_i \tag{8}$$

where $\mathbf{x} = [x \;\; y]^T$ are the global coordinates, $\boldsymbol{\xi} = [\xi \;\; \eta]^T$ are the reference coordinates, ψ_i are the shape functions, and $\mathbf{x}_i$ are the nodal position vectors.

On the parent square, the Q5 interpolation reads

$$\begin{aligned} &\psi_5(\xi,\eta) = (1-\xi^2)(1-\eta^2) \\ &\psi_i(\xi,\eta) = \tfrac{1}{4}\left(1+\xi_i\xi\right)\left(1+\eta_i\eta\right) \\ &\qquad\qquad -\tfrac{1}{4}\psi_5(\xi,\eta), \; i = 1,2,3,4 \end{aligned} \tag{9}$$

with $(\xi_i, \eta_i) \in \{(-1,-1),\ (1,-1),\ (1,1),\ (-1,1)\}$ for the four corners and $(0,0)$ for the center. These functions satisfy partition of unity and the Kronecker property,

$$\begin{aligned} &\sum_{i=1}^{5} \psi_i(\xi,\eta) = 1 \\ &\psi_i(\xi_j,\eta_j) = \delta_{ij}, \;\; (i,j = 1,\ldots,5) \end{aligned} \tag{10}$$

and the global coordinates of the interior node are taken as the centroid of the four corners,

$$(x_5, y_5) = \left(\tfrac{1}{4}\sum_{i=1}^{4} x_i, \tfrac{1}{4}\sum_{i=1}^{4} y_i\right) \tag{11}$$

This enrichment is introduced primarily to improve the kinematic approximation under near-incompressible plane-strain conditions [17, 26, 27]. From a physical and numerical viewpoint, volumetric locking in plane strain arises because, as the material approaches incompressibility, the underlying displacement interpolation becomes overly restrictive: the kinematic space lacks sufficient internal modes to represent nearly isochoric deformation, and the formulation responds with an artificially stiff behavior. In this context, the proposed Q5 interpolation, defined by Eqs. (9)–(11), enriches the standard bilinear approximation through a central bubble-type mode carried by the fifth node with physical displacement DOFs. This additional internal kinematic freedom improves the element's ability to accommodate near-incompressible deformation without resorting to excessive mesh refinement, thereby relaxing spurious volumetric constraints and effectively suppressing locking in plane strain.

3.2. Cell-based smoothed five-node quadrilateral element (CS-FEM-Q5)

Employing the cell-based smoothed strain (CS-FEM) technique [28], instead of Gauss integration, strain measures are obtained by integrating over element-wise smoothing subdomains. Let the computational domain be partitioned into non-overlapping elements $\Omega = \bigcup_{e=1}^{N_e} \Omega_e$. Each element Ω_e is further divided into N_{sc} smoothing cells Ω_k^s, $(k = 1,\ldots,N_{sc})$. Using the Q5 interpolation, the displacement field in an element is approximated by

$$\mathbf{u}^h(\mathbf{x}) = \sum_{i=1}^{5} \psi_i(\mathbf{x})\mathbf{d}_i \tag{12}$$

where ψ_i are the shape functions and $\mathbf{d}_i = [u_i, v_i]^T$ are the nodal displacement vectors.

For a smoothing cell Ω_k^s, the smoothed strain at a sampling point $\mathbf{x}_k$ is defined as

$$\tilde{\boldsymbol{\varepsilon}}^h(\mathbf{x}_k) = \int_{\Omega_k^s} \boldsymbol{\varepsilon}^h(\mathbf{x})\Phi(\mathbf{x})d\Omega \tag{13}$$

where $\tilde{(\cdot)}$ denotes a smoothed quantity and $\Phi(\mathbf{x})$ is a non-negative weight satisfying

$$\int_{\Omega_k^s} \Phi(\mathbf{x})d\Omega = 1$$
$$\Phi(\mathbf{x}) = \begin{cases} 1/A_k, & \mathbf{x} \in \Omega_k^s \\ 0, & \mathbf{x} \notin \Omega_k^s \end{cases} \tag{14}$$

with A_k the area of Ω_k^s.

Applying the divergence theorem gives

$$\begin{aligned} \tilde{\boldsymbol{\varepsilon}}^h(\mathbf{x}_k) &= \frac{1}{A_k}\int_{\Omega_k^s} \boldsymbol{\varepsilon}^h(\mathbf{x})d\Omega \\ &= \frac{1}{A_k}\int_{\Gamma_k^s} \mathbf{n}(\mathbf{x})\mathbf{u}^h(\mathbf{x})d\Gamma \end{aligned} \tag{15}$$

where Γ_k^s is the boundary of Ω_k^s, and $\mathbf{n}$ is the outward unit normal. In 2D,

$$\begin{aligned} \tilde{\boldsymbol{\varepsilon}}^h(\mathbf{x}_k) &= \frac{1}{A_k}\int_{\Omega_k^s} \boldsymbol{\varepsilon}^h(\mathbf{x})d\Omega \\ &= \frac{1}{A_k}\int_{\Gamma_k^s} \mathbf{n}(\mathbf{x})\mathbf{u}^h(\mathbf{x})d\Gamma \\ \mathbf{n}(\mathbf{x}) &= \begin{bmatrix} n_x & 0 \\ 0 & n_y \\ n_y & n_x \end{bmatrix} \end{aligned} \tag{16}$$

Using the finite-element approximation of $\mathbf{u}^h$, the smoothed strain can be written as

$$\tilde{\boldsymbol{\varepsilon}}^h(\mathbf{x}_k) = \sum_{i=1}^{5} \mathbf{B}_i(\mathbf{x})\mathbf{d}_i \tag{17}$$

with the smoothed strain–displacement matrices

$$\mathbf{B}_i(\mathbf{x}) = \begin{bmatrix} \tilde{\psi}_{i,x}(\mathbf{x}) & 0 \\ 0 & \tilde{\psi}_{i,y}(\mathbf{x}) \\ \tilde{\psi}_{i,y}(\mathbf{x}) & \tilde{\psi}_{i,x}(\mathbf{x}) \end{bmatrix} \tag{18}$$

The smoothed derivatives of the shape functions are obtained from a boundary integral over Γ_k^s:

$$\begin{aligned} \tilde{\psi}_{i,\alpha} &= \frac{1}{A_k}\int_{\Gamma_k^s} n_\alpha(\mathbf{x})\psi_i(\mathbf{x})d\Gamma \\ &\approx \frac{1}{A_k}\sum_{j=1}^{n_s} \psi_i(\mathbf{x}_{G_j})n_{\alpha j}l_j \end{aligned} \tag{19}$$

where $\alpha \in \{x, y\}$, n_s is the number of edges of Ω_k^s, $\mathbf{x}_{G_j}$ is the midpoint of edge j^{th}, l_j is its length, and $n_{\alpha j}$ is the corresponding normal component.

As discussed in [26], the choice of the number of smoothing subcells N_{SC} is critical for the near-incompressible plane-strain performance of the CS-FEM-Q5 formulation. In particular, [26] shows that volumetric locking can be effectively suppressed only when $N_{SC} \le 4$. When more than four smoothing subcells are employed, locking may gradually reappear because the smoothing partition effectively increases the incompressibility-related constraints relative to the available kinematic degrees of freedom, leading to an unfavorable DOF-to-constraint ratio (smaller than unity) as analyzed in [26]. Moreover, [26] identifies the four-subcell configuration as the most favorable overall choice, providing the best compromise among locking suppression, convergence, and numerical stability. On the other hand, using fewer smoothing subcells (e.g., one or two) may result in an overly softened response and can trigger spurious zero-energy (hourglass-type) patterns in the kinematic field. For these reasons, the CS-FEM-Q5 discretization with four smoothing subcells per element is adopted in the present study.

4. Numerical discretization

The CS-FEM-Q5 is employed to approximate the displacement field; then, the virtual strain field is calculated by

$$\delta\boldsymbol{\varepsilon} = \mathbf{B}\delta\mathbf{u} \tag{20}$$

where $\delta\mathbf{u}$ is the virtual displacement vector, and $\mathbf{B}$ denotes the smoothed strain-displacement matrix, defined as

$$\mathbf{B} = \begin{bmatrix} \tilde{\psi}_{1,x} & 0 & \tilde{\psi}_{2,x} & 0 & \cdots & \tilde{\psi}_{N,x} & 0 \\ 0 & \tilde{\psi}_{1,y} & 0 & \tilde{\psi}_{2,y} & \cdots & 0 & \tilde{\psi}_{N,y} \\ \tilde{\psi}_{1,y} & \tilde{\psi}_{1,x} & \tilde{\psi}_{2,y} & \tilde{\psi}_{2,x} & \cdots & \tilde{\psi}_{N,y} & \tilde{\psi}_{N,x} \end{bmatrix} \tag{21}$$

where N denotes the number of nodes, and $\tilde{\psi}_{i,x}$, $\tilde{\psi}_{i,y}$ are the smoothed derivatives of the shape function at node i.

The weak form of the residual-stress equilibrium can be written via numerical integration as

$$\int_{\Omega}\left[\mathbf{B}\delta\mathbf{u}\right]^{T}\boldsymbol{\sigma}^{r}\,d\Omega = \delta\mathbf{u}^{T}\int_{\Omega}\mathbf{B}^{T}\boldsymbol{\sigma}^{r}\,d\Omega = \delta\mathbf{u}^{T}\sum_{k=1}^{N_s}A_k\mathbf{B}_k^{T}\boldsymbol{\sigma}_k^{r} = 0 \tag{22}$$

where N_s is the number of smoothing domains and A_k is the area of the k^{th} smoothing domain.

Since the above must hold for all $\delta\mathbf{u}$, it follows that

$$\sum_{k=1}^{N_s}A_k\mathbf{B}_k^{T}\boldsymbol{\sigma}_k^{r} = \mathbf{C}\boldsymbol{\sigma}^{r} = \mathbf{0} \tag{23}$$

where $\mathbf{C}$ is the assembled constant equilibrium matrix, which enforces essential boundary conditions by removing the corresponding degrees of freedom on kinematic boundaries.

The fictitious stress in each smoothing domain is computed by the standard Galerkin relation

$$\boldsymbol{\sigma}_k^{e} = \mathbf{D}\mathbf{B}_k\mathbf{u}_k \tag{24}$$

where $\mathbf{D}$ is the constitutive matrix. It is emphasized that the bubble enrichment increases the total number of degrees of freedom in this auxiliary step; however, it does not affect the total number of variables in the final (limit-analysis) step, since the residual stress field becomes the primary unknown and the stress constraints are enforced at the CS-FEM integration points (i.e., the smoothing domains).

Finally, once the auxiliary variable $\boldsymbol{\rho}$ is determined and the yield condition is enforced over all smoothing domains, the pseudo-lower-bound problem can be written as:

$$\lambda^{-} = \max\ \lambda$$
$$\text{s.t.}\quad \begin{cases}\mathbf{C}\boldsymbol{\sigma}^{r} = \mathbf{0}\\ \boldsymbol{\rho}_k \in \mathcal{C}_k,\ k = 1,2,\ldots,N_s\end{cases} \tag{25}$$

It is worth noting that the load multiplier obtained from Eq. (25) should be interpreted as a pseudo–lower-bound estimate rather than a strict lower bound in the classical sense of limit analysis. Although Eq. (25) is motivated by Melan’s static (lower-bound) theorem, the admissible stress field is not constructed as an independent, pointwise equilibrated field. In the present formulation, the fictitious elastic stress is evaluated from a kinematic approximation (the virtual displacement field), and the equilibrium conditions associated with the lower-bound problem are imposed only in a weak, spatially averaged sense over the CS-FEM smoothing domains. As a result, the constraints are satisfied in an integral (smoothed) manner rather than pointwise, and the reconstructed stress field may not be strictly statically admissible everywhere. Therefore, the computed multiplier is not guaranteed to be on the safe side for all discretizations; depending on the kinematic approximation used to recover the fictitious elastic stress, the numerical response may even display an upper-bound–like convergence trend. We thus use the term “pseudo–lower-bound” to emphasize that Eq. (25) is rooted in the lower-bound framework but does not provide a rigorous lower-bound guarantee. Nevertheless, with a sufficiently fine discretization, the proposed scheme can still provide a practically reliable load multiplier, with a sufficiently small deviation from reference (exact) solutions for typical engineering problems.

Post-processing and collapse mechanism identification.

After solving the SOCP problem for the limit analysis, the total stress quantities are recovered at the smoothing domains and used to construct a scalar equivalent-stress field for visualization. In particular, for each smoothing subcell, the equivalent (von Mises) stress is extracted directly from the SOCP solution via the auxiliary cone variables introduced in Eq. (4). For plane stress, the equivalent stress is computed as

$$\sigma_{eq} = \sqrt{\rho_2^2 + \rho_3^2 + \rho_4^2} \tag{26}$$

whereas for plane strain it is evaluated as

$$\sigma_{eq} = \sqrt{\rho_2^2 + \rho_3^2} \tag{27}$$

This yields an equivalent-stress field at the smoothing domains, denoted by $\sigma_{eq}^{(k)}$ for the k^{th} smoothing subcell. The field is then mapped to the element level by an area-weighted average over the subcells of each element

$$\sigma_{eq}^{e} = \frac{\sum_{i=1}^{N_{sc}} \sigma_{eq}^{(k)} A^{(k)}}{\sum_{i=1}^{N_{sc}} A^{(k)}} \tag{28}$$

where N_{sc} is the number of smoothing subcells per element and $A^{(k)}$ is the area of the k^{th} subcell. Finally, a nodal field is constructed by averaging the element-wise values over all elements sharing the nodes

$$\sigma_{eq}^{i} = \frac{\sum_{e\in\Re(i)} \sigma_{eq}^{e} A^{e}}{\sum_{e\in\Re(i)} A^{e}} \tag{29}$$

where $\Re(i)$ denotes the set of elements adjacent to node i^{th} and A^{e} is the area of element e. The collapse mechanism is then inferred from the normalized nodal equivalent-stress field $\sigma_{eq}^{i} / \sigma^{p}$ by marking the connected regions where this indicator attains (or closely approaches) unity; the resulting high-stress bands delineate the dominant collapse mechanism.

5. Numerical results

This section presents a numerical investigation of a benchmark problem: a thin square plate with a central circular cutout subjected to biaxial in-plane pressure. The hole radius-to-plate length ratio is 0.2. The material properties $E = 2.1\times10^{5}$ MPa, $\nu = 0.49999$, and $\sigma^{p} = 250$ MPa. Exploiting geometric and loading symmetry, only the upper-right quarter of the plate is modeled. The computational domain ($R = 1$m, $A = 5$ m) is shown in Fig. 1(a), and the Q5-element finite-element mesh is shown in Fig. 1(b).

Under plane stress, the uniaxial loading case $(p_1 \neq 0, p_2 = 0)$ with a known analytical solution is first examined to verify the convergence behavior and accuracy of the proposed approach. The results are reported in Table 1 and illustrated in Fig. 2(a). As the number of elements increases, the present pseudo-lower-bound solution converges to the analytical value from above, exhibiting the same qualitative convergence trend as upper-bound formulations. In this study the pseudo-lower-bound framework is employed, wherein the virtual displacement field is approximated, and static equilibrium is enforced in a weak sense; this accounts for the observed convergence trend. In terms of accuracy, the mesh with 6,400 elements yields $\lambda = 0.8008$, corresponding to a 0.1% deviation from the analytical solution $\lambda = 0.8000$ reported by Gaydon and McCrum [29]. Furthermore, the optimization timings in Table 1 indicate computational efficiency: the problem with 179,201 variables is solved in 2.52 s, underscoring the robustness and effectiveness of the proposed method.

To evaluate the proposed method's ability to alleviate volumetric locking, CS-FEM with a standard quadrilateral mesh (CS-FEM-Q4) is used as a comparator; both discretizations use four smoothing sub-cells per element. Under plane-stress loading (Fig. 2a), CS-FEM-Q4 already performs well, with accuracy only slightly below that of the Q5-enriched variant. In plane strain (Fig. 2b), however, Q4 shows the familiar symptoms of locking–its solutions stagnate and deviate from the reference trends reported by Garcea et al. [30]–whereas CS-FEM-Q5 remains locking-free and converges consistently to those references across all tested cases.

It is also worth noting that the above plane-strain study already considers an extremely near-incompressible value ($\nu = 0.49999$). Additional calculations performed with lower Poisson's ratios exhibit essentially unchanged convergence trends and collapse multipliers. This observation is consistent with the adopted pseudo–lower-bound setting. Poisson's ratio affects only the auxiliary linear-elastic reconstruction of the fictitious stress field, while the residual stress, serving as the primary SOCP unknown, redistributes so that the resulting total stress remains statically admissible. Because the virtual displacement field is approximated and equilibrium is enforced in a weak sense, the formulation does not constitute a strict lower-bound statement; consequently, locking effects commonly seen in upper-bound approximations can still appear. In practice, however, the CS-FEM-Q5 discretization suppresses volumetric locking effectively in near-incompressible plane strain, leading to reliably lower errors, smoother convergence, and stable, reference-consistent collapse multipliers, with only a modest increase in degrees of freedom in the auxiliary fictitious-stress reconstruction step (due to the added bubble-node kinematic DOFs), while the size of the final SOCP optimization problem remains governed by the number of smoothing domains.

Table 2 compares the present collapse multipliers with classical references for three load cases. In plane stress, our values fall within the published range and differ by only a few tenths of a percent from the analytical solution for the first case and from the most cited numerical results for the second and third cases. In plane strain, for the first case, our multiplier essentially coincides with Ho et al. [26] and with locking-tolerant LT/SP triangular discretizations [30], while remaining well below the constant-strain (CT) value [30]–consistent with the known overestimation caused by volumetric locking in CT elements. For the combined-loading plane-strain cases, the only published results are those of Ho et al. [26]; our values coincide with theirs to four decimal places. Overall, the present formulation reproduces established plane-stress benchmarks and yields plane-strain multipliers consistent with locking-resistant discretizations, while avoiding the CT-triangle overestimation. The plate's collapse mechanisms, identified from the distribution of the normalized plastic stress field at the limit state under various loading conditions, are shown in Figs. 3 and 4.

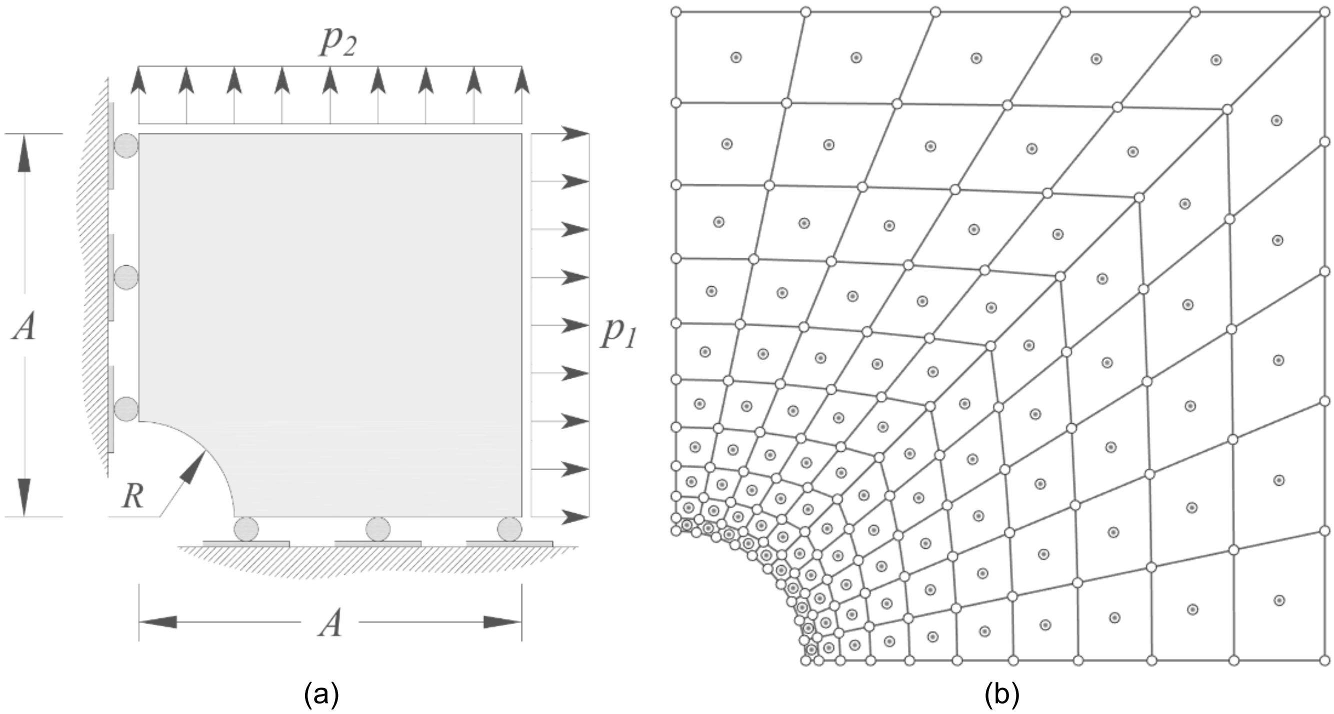

Fig. 1. Plate hole: (a) computational domain showing geometry, dimensions, boundary conditions, and loading; (b) finite-element discretization using CS-FEM-Q5

Table 1. Plate hole (plane stress, $(p_1 \neq 0,\ p_2 = 0)$: computed limit load multipliers

N_e	N_{var}	λ^-	e (%)	Time (s)
400	11,201	0.8037	0.46	0.11
1,600	44,801	0.8017	0.21	0.43
3,600	100,801	0.8011	0.13	1.16
6,400	179,201	0.8008	0.10	2.52

N_e : number of elements; N_{var} : number of variables; e (%): relative error.

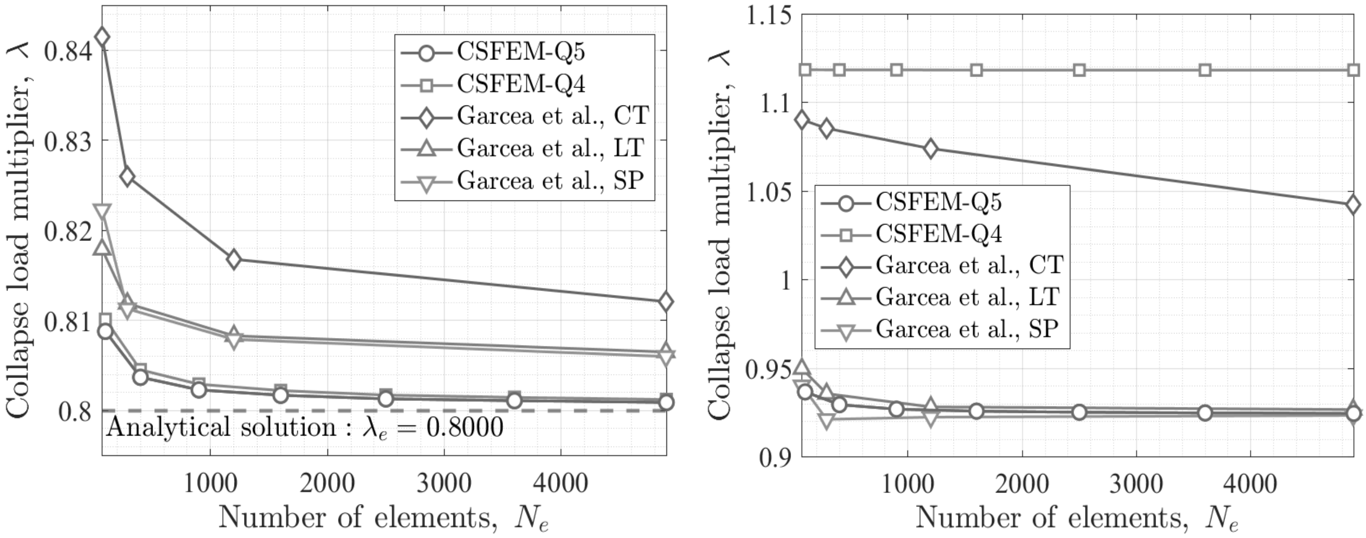

(a) Plane stress (b) Plane strain

Fig. 2. Plate hole $(p_1 \neq 0,\ p_2 = 0)$: convergence analysis of solutions

Table 2. Plate hole: comparison with other studies

Author	Plane stress			Plane strain		
	$p_2 = 0$	$p_1 = 2p_2$	$p_1 = p_2$	$p_2 = 0$	$p_1 = 2p_2$	$p_1 = p_2$
Present study	0.8008	0.911	0.895	0.9243	1.4483	1.8606
Groβ-Weege [31]	0.7920	0.891	0.882	-	-	-
Zouain et al. [32]	0.8030	0.911	0.894	-	-	-
da Silva & Antao [33]	0.8070	0.915	0.899	-	-	-
Le et al. [16]	0.8010	0.911	0.895	-	-	-
Chen et al. [34]	0.7980	0.899	0.874	-	-	-
Ho & Le [35]	0.8001	0.902	0.871	-	-	-
Ho et al. [36]	0.8007	0.911	0.896	-	-	-
Ho et al. [23], UB	0.8001	0.910	0.895	0.9232	-	-
Ho et al. [23], pLB	0.8000	0.910	0.895	0.9232	-	-
Ho et al. [26]	0.8008	0.911	0.896	0.9244	1.4484	1.8607
Garcea et al. [30], CT	0.8121	-	-	1.0424	-	-
Garcea et al. [30], LT	0.8065	-	-	0.9267	-	-
Garcea et al. [30], SP	0.8060	-	-	0.9234	-	-

CT: constant strain elements; LT: linear strain elements; SP: simplex elements; UB: upper bound; pLB: pseudo-lower-bound.

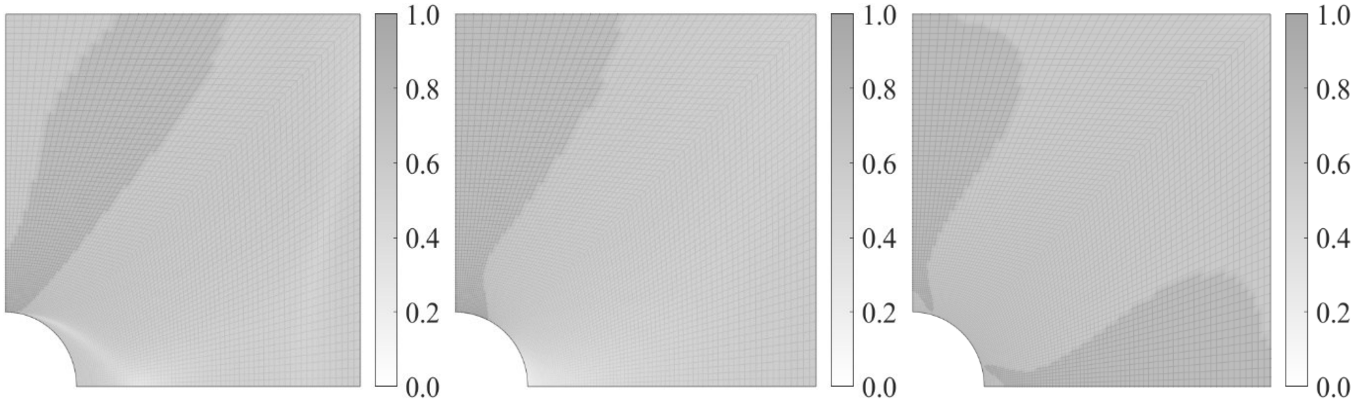

(a) $p_1 \neq 0,\ p_2 = 0$ (b) $p_1 = 2p_2$ (c) $p_1 = p_2$

Fig. 3. Plate hole (plane stress): plastic stress distribution at the limit state under various loading combinations

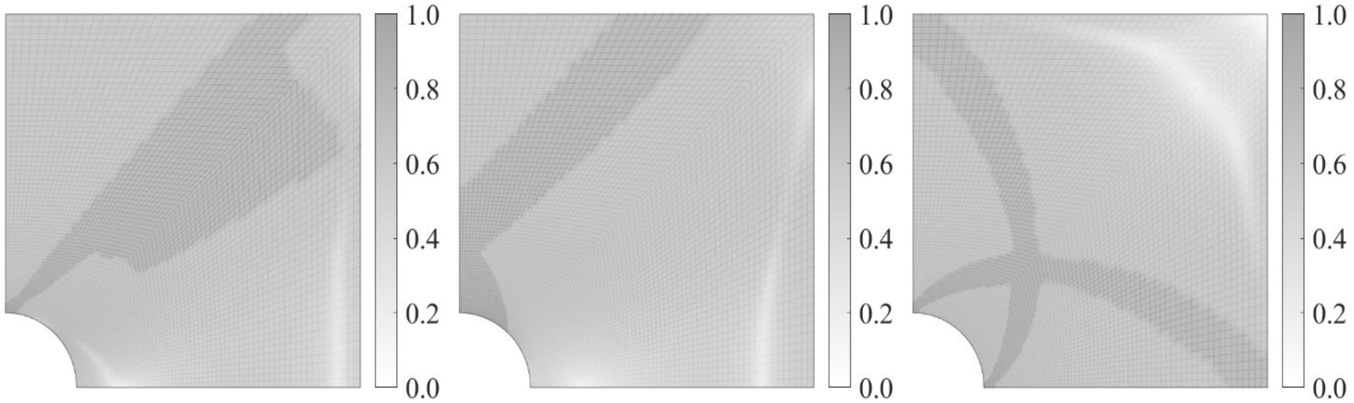

(a) $p_1 \neq 0,\ p_2 = 0$ (b) $p_1 = 2p_2$ (c) $p_1 = p_2$

Fig. 4. Plate hole (plane strain): plastic stress distribution at the limit state under various loading combinations

6. Conclusions

A locking-free, pseudo-lower-bound limit-state formulation, where a bubble-enriched conforming quadrilateral (Q5) is coupled with cell-based strain smoothing (CS-FEM-Q5), has been presented. The element-level enrichment introduces a single interior node while retaining conformity, and the smoothing over cell partitions allows equilibrium to be enforced in a weak, spatially averaged sense using a decomposition of the plastic stress into fictitious elastic and residual parts. Although the proposed formulation yields a pseudo–lower-bound estimate (which may occasionally exceed the exact collapse load), a sufficiently refined discretization typically produces highly accurate results with very small errors for practical engineering problems; hence, it can be used in engineering design provided that an appropriate safety factor is adopted.

Numerical studies on plane-strain benchmarks indicate that the approach suppresses volumetric locking, delivers accurate collapse multipliers and mechanisms, and exhibits consistent convergence under mesh refinement. The SOCP structure enables efficient solutions with modern conic optimizers, making the method suitable for design-oriented computations. Future work will target extensions to three-dimensional settings, generalized loading paths (e.g., shakedown), complex constitutive behaviors, and adaptive smoothing/meshing strategies.

Acknowledgments

This research is funded by the Vietnam Ministry of Science and Technology under grant number ĐTĐLCN.03/25.

Declaration of Generative AI

During the preparation of this work, the authors used Grammarly and ChatGPT (OpenAI) in order to improve the readability and language of the manuscript. After using these tools, the authors reviewed and edited the content as needed and take full responsibility for the content of the published article.

References

[1]. R. Hill. (1951). LXXXVIII. On the state of stress in a plastic-rigid body at the yield point. *The London, Edinburgh, and Dublin Philosophical Magazine and Journal of Science*, 42(331), 868–875. https://doi.org/10.1080/14786445108561315

[2]. D.C. Drucker, W. Prager, H.J. Greenberg. (1952). Extended limit design theorems for continuous media. *Quarterly of Applied Mathematics*, 9, 381–389. https://doi.org/10.1090/qam/45573

[3]. A.A. Gvozdev. (1960). The determination of the value of the collapse load for statically indeterminate systems undergoing plastic deformation. *International Journal of Mechanical Sciences*, 1(4), 322–335. https://doi.org/10.1016/0020-7403(60)90051-5

[4]. E. Melan. (1938). On the Plasticity of the Spatial Continuum (in German). *Ingenieur-Archiv*, 9, 116–126. https://doi.org/10.1007/BF02084409

[5]. W.T. Koiter. (1960). General theorems for elastic-plastic solids. *Progress in Solid Mechanics*, 1, 165–221. *North-Holland Publisher.* https://cir.nii.ac.jp/crid/1573105974892560896

[6]. J.C. Nagtegaal, D.M. Parks, J.R. Rice. (1974). On numerically accurate finite element solutions in the fully plastic range. *Computer Methods in Applied Mechanics and Engineering*, 4(2), 153–177. https://doi.org/10.1016/0045-7825(74)90032-2

[7]. T.J.R. Hughes. (1987). The finite element method: Linear static and dynamic finite element analysis. *Prentice-Hall, Inc., USA.*

[8]. F. Tin-Loi, N.S. Ngo. (2003). Performance of the p-version finite element method for limit analysis. *International Journal of Mechanical Sciences*, 45(6–7), 1149–1166. https://doi.org/10.1016/j.ijmecsci.2003.08.004

[9]. S.W. Sloan, M.F. Randolph. (1982). Numerical prediction of collapse loads using finite element methods. *International Journal for Numerical and Analytical Methods in Geomechanics*, 6(1), 47–76. https://doi.org/10.1002/nag.1610060105

[10]. C.V. Le, H. Askes, M. Gilbert. (2012). A locking-free stabilized kinematic EFG model for plane strain limit analysis. *Computers & Structures*, 106-107, 1–8. https://doi.org/10.1016/j.compstruc.2012.03.012

[11]. P.L.H. Ho, C.V. Le, T. Tran-Cong. (2016). Displacement and equilibrium mesh-free formulation based on integrated radial basis functions for dual yield design. *Engineering Analysis with Boundary Elements*, 71, 92–100. https://doi.org/10.1016/j.enganabound.2016.07.010

[12]. E. Christiansen, K.D. Andersen. (1999). Computation of collapse states with von Mises type yield condition. *International Journal for Numerical Methods in Engineering*, 46(8), 1185–1202. https://doi.org/10.1002/(SICI)1097-0207(19991120)46:8<1185::AID-NME743>3.0.CO;2-N

[13]. A. Capsoni, L. Corradi. (1997). A finite element formulation of the rigid–plastic limit analysis problem. *International Journal for Numerical Methods in Engineering*, 40(11), 2063–2086. https://doi.org/10.1002/(SICI)1097-0207(19970615)40:11<2063::AID-NME159>3.0.CO;2-%23

[14]. S.W. Sloan, P.W. Kleeman. (1995). Upper bound limit analysis using discontinuous

velocity fields. *Computer Methods in Applied Mechanics and Engineering*, 127(1–4), 293–314. https://doi.org/10.1016/0045-7825(95)00868-1

[15]. A. Makrodimopoulos, C.M. Martin. (2007). Upper bound limit analysis using simplex strain elements and second-order cone programming. *International Journal for Numerical and Analytical Methods in Geomechanics*, 31(6), 835–865. https://doi.org/10.1002/nag.567

[16]. C.V. Le, H. Nguyen-Xuan, H. Askes, S.P.A. Bordas, T. Rabczuk, H. Nguyen-Vinh. (2010). A cell-based smoothed finite element method for kinematic limit analysis. *International Journal for Numerical Methods in Engineering*, 83(12), 1651–1674. https://doi.org/10.1002/nme.2897

[17]. C.T. Wu, W. Hu, J.S. Chen. (2012). A meshfree-enriched finite element method for compressible and near-incompressible elasticity. *International Journal for Numerical Methods in Engineering*, 90(7), 882–914. https://doi.org/10.1002/nme.3349

[18]. C.T. Wu, W. Hu. (2012). A two-level mesh repartitioning scheme for the displacement-based lower-order finite element methods in volumetric locking-free analyses. *Computational Mechanics*, 50, 1–18. https://doi.org/10.1007/s00466-011-0665-7

[19]. H. Nguyen-Xuan, C.T. Wu, G.R. Liu. (2016). An adaptive selective ES-FEM for plastic collapse analysis. *European Journal of Mechanics – A/Solids*, 58, 278–290. https://doi.org/10.1016/j.euromechsol.2016.02.005

[20]. H. Nguyen-Xuan, G.R. Liu. (2013). An edge-based smoothed finite element method softened with a bubble function (bES-FEM) for solid mechanics problems. *Computers & Structures*, 128, 14–30. https://doi.org/10.1016/j.compstruc.2013.05.009

[21]. P.L.H. Ho, C.V. Le, C. Lee, D.T. Tran, P.H. Nguyen, J.-J. Yee. (2024). Dual failure analysis of 3D structures under cyclic loads using bFS-FEM based numerical approaches. *Finite Elements in Analysis and Design*, 242, 104272. https://doi.org/10.1016/j.finel.2024.104272

[22]. P.L.H. Ho, C. Lee, C.V. Le, P.H. Nguyen, J.-J. Yee. (2024). A computational homogenization for yield design of asymmetric microstructures using adaptive bES-FEM. *Computers & Structures*, 294, 107271. https://doi.org/10.1016/j.compstruc.2023.107271

[23]. P.L.H. Ho, C. Lee, C.V. Le, D.T. Tran, P.H. Nguyen, J.-J. Yee. (2025). Dual bubble-enriched SFEM approaches for locking-free analysis of structures under cyclic loads. *International Journal of Applied Mechanics*, 17(3), 2550002. https://doi.org/10.1142/S1758825125500024

[24]. C. Lee, P.L.H. Ho, S. Natarajan, C.V. Le, J.-J. Yee. (2025). Polytree-based adaptive bubble-enriched smoothed polygonal finite element method for dual yield structural design. *Engineering with Computers*, 41, 3071–3097. https://doi.org/10.1007/s00366-025-02150-y

[25]. Y. Zhang, S. Wang, D. Chan. (2014). A new five-node locking-free quadrilateral element based on smoothed FEM for near-incompressible linear elasticity. *International Journal for Numerical Methods in Engineering*, 100(9), 633–668. https://doi.org/10.1002/nme.4754

[26]. P.L.H. Ho, C. Lee, C.V. Le, J.-J. Yee. (2025). Shakedown analysis of incompressible materials under cyclic loads: A locking-free CS-FEM-Q5 numerical approach. *International Journal of Non-Linear Mechanics*, 168, 104932. https://doi.org/10.1016/j.ijnonlinmec.2024.104932

[27]. U. Hueck, H.L. Schreyer, P. Wriggers. (1995). On the incompressible constraint of the 4-node quadrilateral element. *International Journal for Numerical Methods in Engineering*, 38(18),

3039–3053. https://doi.org/10.1002/nme.1620381803

[28]. G.R. Liu, K.Y. Dai, T.T. Nguyen. (2007). A smoothed finite element method for mechanics problems. *Computational Mechanics*, 39, 859–877. https://doi.org/10.1007/s00466-006-0075-4

[29]. F.A. Gaydon, A.W. McCrum. (1954). A theoretical investigation of the yield point loading of a square plate with a central circular hole. *Journal of the Mechanics and Physics of Solids*, 2(3), 156–169. https://doi.org/10.1016/0022-5096(54)90022-8

[30]. G. Garcea, G. Armentano, S. Petrolo, R. Casciaro. (2005). Finite element shakedown analysis of two-dimensional structures. *International Journal for Numerical Methods in Engineering*, 63(8), 1174–1202. https://doi.org/10.1002/nme.1316

[31]. J. Groβ-Weege. (1997). On the numerical assessment of the safety factor of elastic-plastic structures under variable loading. *International Journal of Mechanical Sciences*, 39(4), 417–433. https://doi.org/10.1016/S0020-7403(96)00039-2

[32]. N. Zouain, L. Borges, J.L. Silveira. (2002). An algorithm for shakedown analysis with nonlinear yield functions. *Computer Methods in Applied Mechanics and Engineering*, 191(23–24), 2463–2481. https://doi.org/10.1016/S0045-7825(01)00374-7

[33]. M.V. da Silva, A.N. Antão. (2007). A non-linear programming method approach for upper bound limit analysis. *International Journal for Numerical Methods in Engineering*, 72(10), 1192–1218. https://doi.org/10.1002/nme.2061

[34]. S. Chen, Y. Liu, Z. Cen. (2008). Lower-bound limit analysis by using the EFG method and non-linear programming. *International Journal for Numerical Methods in Engineering*, 74(3), 391–415. https://doi.org/10.1002/nme.2177

[35]. P.L.H. Ho, C.V. Le. (2020). A stabilized iRBF mesh-free method for quasi-lower bound shakedown analysis of structures. *Computers & Structures*, 228, 106157. https://doi.org/10.1016/j.compstruc.2019.106157

[36]. P.L.H. Ho, C.V. Le, T.Q. Chu. (2019). The equilibrium cell-based smooth finite element method for shakedown analysis of structures. *International Journal of Computational Methods*, 16(5), 1840013. https://doi.org/10.1142/S0219876218400133